Lab on a Chip

PAPER

View Article Online
View Journal | View Issue

Cite this: *Lab Chip*, 2024, 24, 3294

On-demand drug delivery bioelectronics through a water-processable low dimensional highly conductive MXene layer†

Hyeok-jin Kwon, ‡[ab] Yizhang Wu, ‡[a] Yuan Li,[c] Gongkai Yuan,[a] Rene Lopez,[a] Ke Huang[c] and Wubin Bai*[a]

Received 15th March 2024,
Accepted 31st May 2024

DOI: 10.1039/d4lc00234b

rsc.li/loc

On-demand drug delivery holds great promise to optimize pharmaceutical efficacy while minimizing the side effects. However, existing on-demand drug delivery systems often require complicated manufacturing processes that preclude their wide implementation of a broad range of drugs. In this work, we demonstrate the introduction of MXene-coated microneedles (MNs) into bioelectronics for digitally controllable gate-valve drug delivery. MXenes, featuring high electronic conductivity, excellent biocompatibility, and solution processibility, enable low-cost scalability for printable bioelectronics. In an electrolytic state (*e.g.*, body fluid), the coated MXene is oxidized and desorbed due to redox reactions caused by electrical bias, allowing the underlying drug to be controllably released. The MXene-incorporated drug delivery system not only demonstrates excellent biocompatibility and operational stability, but also features low-cost construction and sustainable usage. Besides, these MXene-coated MNs allow both on-demand transformation and local-region customization, further increasing the structural versatility and capability of multidrug delivery systems.

1. Introduction

Active systems offering precise drug delivery on-demand hold great promise to enhance pharmaceutical efficacy, minimize side effects, and improve user adherence.[1,2] However, existing technologies for on-demand drug delivery with substantial spatiotemporal precision mostly require complicated manufacturing approaches and/or specialized processing environments, which not only increases costs but also limits the choices of drugs that are compatible with the packaging processes.[3–5] Microneedles (MNs), composed of submillimeter-sized protrusion (50 to 900 μm) arrays,[6,7] can enable drug delivery beneath the epidermis without disrupting the cutaneous nerve network.[8] When MNs penetrate the skin layer, microchannels are formed to realize the in-body drug diffusion complying with coat-and-poke technology, which increases the permeability and absorption of the drug.[9] Existing efforts on MN drug delivery have been primarily focusing on controlling the rate of drug release that is simultaneously influenced by the in-body microenvironment (pH, temperature, and/or biochemical potentials), which, however, cannot be tightly controlled externally and often encounter inconsistencies in responding to subtle variations in the trigger factors.[10,11] The grand challenges remain mostly on developing a scalable strategy for actively controlled drug delivery that is compatible for loading a broad range of drugs.

Biocompatible metallic materials that undergo crevice reactions in biofluids upon a voltage trigger can serve as actively controlled gates for electrically controlled drug-delivery systems, enabling customizable, programmable control over the timing of release events.[12,13] MXene is a term for layered transition metal compounds of intrinsic metallicity.[14] MXenes constitute a large family of compounds and can be represented as $M_{n+1}X_nT_x$ (n = 1–3), where "M" is an early transition metal, "X" is carbon or nitrogen, and "T" stands for the hydrophilic surface terminations (–O–, –F, and –OH). The hydrophilic termination of MXene is able to form water-dispersed MXene solutions.[15] This property allows MXene solutions to be easily processed into thin films for a variety of conductive layer-based applications with water processes.[16] Additionally, they have high electrical conductivity, antibacterial properties, biocompatibility and acid/base resistance.[17,18] In the existing literature, pathological toxicity, side effects, and inflammation

[a] *Department of Applied Physical Sciences, University of North Carolina at Chapel Hill, Chapel Hill, NC 27599, USA. E-mail: wbai@unc.edu*
[b] *Department of Industrial Chemistry, Pukyong National University, Busan 48513, Republic of Korea*
[c] *Joint Department of Biomedical Engineering, at University of North Carolina Chapel Hill, and North Carolina State University, Raleigh, North Carolina, 27607, USA*

† Electronic supplementary information (ESI) available. See DOI: https://doi.org/10.1039/d4lc00234b

‡ These authors equally contributed.

were rarely observed when using MXene-based treatments.[19,20] In contrast to MNs based on conventional metals (*e.g.*, gold, platinum, and iridium) where the fabrication process is implemented on finite-size wafers or in a cleanroom facility, MXenes, featuring water-solubility, can be more amenable to streamlined manufacturing processes.[21] This amenability opens the possibility of implementing roll-to-roll manufacturing methods, facilitating customizable and low-cost scalability.[22]

In this work, an MXene-incorporated MN array is fabricated to implement the strictly controlled release of drugs. Briefly, this system, following the galvanic corrosion theory, utilizes the decomposition voltage of intrinsic metallic MXene coating to open the gate, actively enabling immediate and rapid drug delivery. Meanwhile, the MXene-based probes show impressive biocompatibility and biostability in a biofluid environment for two weeks. This confirms the potential of MXene coating for long-term MN deployment. Besides, the solution-processable MXene layer achieves on-demand transformation and local-region customization with low-cost scalability.

2. Results & discussion

Fig. 1 illustrates the schematics of MXene-coated MNs as drug carriers and activation. The substrate for the MNs is ethyl cellulose, a cellulose derivative notable for its low water solubility and excellent biocompatibility.[23,24] The comprehensive process of MN manufacturing is depicted in Fig. S1.† Initially, a microneedle mold was crafted from polydimethylsiloxane (PDMS), employing a laser writer and UV laser irradiation (~254 nm). Subsequently, the ethyl cellulose solution (~10 wt%) was meticulously cast onto the dust-free surface of the PDMS mold, following an evacuation process under mild vacuum and low-temperature conditions (~50 °C) for 10 minutes. Vacuum venting enables the thorough filling of the mold cavities with the ethyl cellulose solution. The solution was then allowed to dry under ambient air conditions for 24 hours, facilitating the complete evaporation of the remaining solvent and resulting in the formation of the MN structure with ethyl cellulose. The MN arrays, comprising 5 × 5 microneedles with each conical cavity measuring 150 μm in base diameter, 550 μm in height,

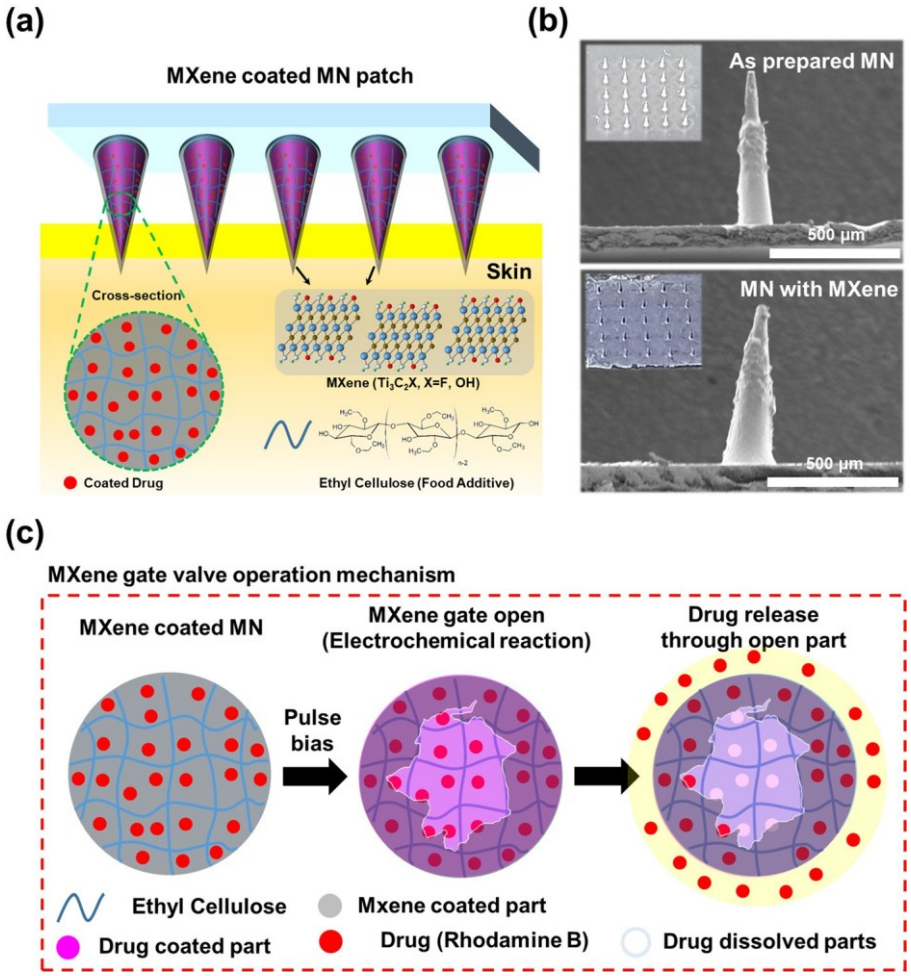

Fig. 1 (a) Schematic illustration of ethyl cellulose MN patch application, (b) photograph and cross-section SEM image of MNs without/with MXene coating, and (c) operation steps of drug release in MXene/drug coated MN bioelectronics.

and 1000 μm in tip-to-tip spacing, were then gently detached from the mold. The scanning electron microscope (SEM) image in Fig. S1† presents a detailed view of these fabricated MN patches.

Fig. 1a schematically shows a demonstrative application of the drug delivery system toward skin with the MXene-coated MN patch. As mentioned earlier, ethyl cellulose has a certain degree of resistance to water, so the three-dimensional structure produced with ethyl cellulose can be maintained even if a water-based solution process is applied.[25] Therefore, water-soluble rhodamine B (RhB) or other dye materials, as model drugs, were firstly coated onto the ethyl cellulose base MN patches, and MXene, as an electrochemical gate valve/stimuli-responsive material, was secondly coated on the drug-loaded MN patches through a drop-casting process. Unlike the dip coating process,[26] because the solution is applied directly on the coated layer, MXene successfully covers water-soluble drugs, except that some drugs in the surface layer are dissolved. As shown in the photo in Fig. 1b, MXene layers were successfully coated on the ethyl cellulose-based MNs through a water-based solution process. Water is the representative green solvent that comes to mind when thinking of solvent–solute mixtures. In this respect, the aqueous solution processing makes the bioelectronics manufacturing safe for bioapplications and inclusive for loading a broad range of drugs.[27,28]

Fig. 1b and S2a and b† illustrate the SEM images, revealing that the fundamental structure of the MNs is preserved both before and after the MXene coating. Energy-dispersive X-ray spectroscopy (EDX) analysis provides atomic component distribution maps, confirming the uniform deposition of MXene on the ethyl cellulose-based MNs. Titanium (Ti), the principal atomic component of MXene ($Ti_{n+1}C_nT_x$), is virtually absent in the MN sample. However, following the MXene coating, Ti is prominently distributed on the surface, surpassing the concentration of carbon (C). Despite the preservation of the micrometer-scale shape, there are noticeable changes in surface morphology post-MXene application. SEM images depicted in Fig. S3a† highlight these morphological changes. The as-prepared MNs display a highly rough surface due to the polymer structure. In contrast, MNs coated with MXene exhibit a relatively smooth surface, suggesting a complete encapsulation by MXene. Notably, several aggregated MXenes, characterized by an overlapping layered structure, are observed on the surface, as shown in Fig. S3b.†[29]

Fig. 1c briefly shows the operation mechanism of on-demand drug release in our work. We utilized the stimuli-responsive material MXene, which can undergo electrochemical degradation upon a trigger of voltage bias applied when the system is biofluid/phosphate buffer solution (PBS). Application of an electrical bias larger than 1.0 V toward the MXene coating can cause crevice degradation, then exposing the water-soluble drugs covered underneath and releasing them to areas affected by the illness. Therefore, the bioelectronics we fabricated were devices for electrochemical drug delivery release control with MXene materials and MNs. The materials used in various previously reported gate valve-type drug delivery bioelectronics were general metal materials (Mg, Mo, *etc.*).[12,13] Compared to existing materials that have been manufactured through a vacuum process, MXene materials can be easily manufactured through a solution process and have the advantage of minimizing drug loss due to the vacuum process. MXene also features quite excellent conductivity like metallic materials, but it was necessary to check whether degradation due to oxidation and reduction occurs under electrochemical conditions like metallic materials in this system.

Fig. 2a schematically illustrates that MXene ($Ti_3C_2T_x$) can function as a gate valve system.[12,13] For $Ti_3C_2T_x$, utilizing the MXene series in this study, it is usually reported that the interaction of water and dissolved oxygen with flake edges and defects causes oxidation to generate TiO_2 nuclei, which grow and spread throughout the surface.[30,31] However, $Ti_3C_2T_x$ in aqueous solution by hydration chemistry of inorganic salts with nontoxicity, abundant reserve, and low cost (*e.g.*, NaCl, LiCl, and $CaCl_2$) under ambient conditions (very similar to body fluid conditions) makes the long-term storage possible.[32] Salts in an aqueous solution reduce the proportion of free water molecules in the solution and their interaction with MXene. On the other hand, when an electrical bias is applied to MXene, a redox phenomenon occurs between water and MXene, forming and spreading TiO_2 nuclei throughout the surface.

Fig. 2b shows the pristine MXene thin film deposited on bare glass substrates in order to investigate the redox properties of MXene. The as-fabricated sample with copper tape, was integrated into a simple electrolytic cell, opposite to another pristine copper tape immersed in a PBS solution. Notably, the inset in Fig. 2b depicts the oxidation of the MXene layers' dipped region after applying a static direct current (DC) to the circuit. Fig. 2c shows the effects of applied voltage and the resistance of the MXene layer (reflected in the thickness) on the decomposition time, as determined using an electrochemical analyzer. The left graph in Fig. 2c elucidates the corrosion current per unit area as a function of time for various applied voltages, with 200 Ω original resistance of the MXene layer between two points (depicted in Fig. S4†). According to the graph, the current decreases at first. As the electrochemical reaction occurs, gas is generated on the surface, and the measured current value decreases due to a decrease in the efficiency of the current. As the electrochemical reaction progresses, the decomposition of the MXene layer leads to regional insulation with a clear contrast between the impregnated and non-impregnated parts.[12] This causes a second inflection point over time (shown as arrows in the graph), at which point the drug is discharged to the outside through the gate valve for drug delivery. In particular, the rate of degradation is strongly determined by the Faraday laws that the injected charge is converted into an oxidation product or a reduction

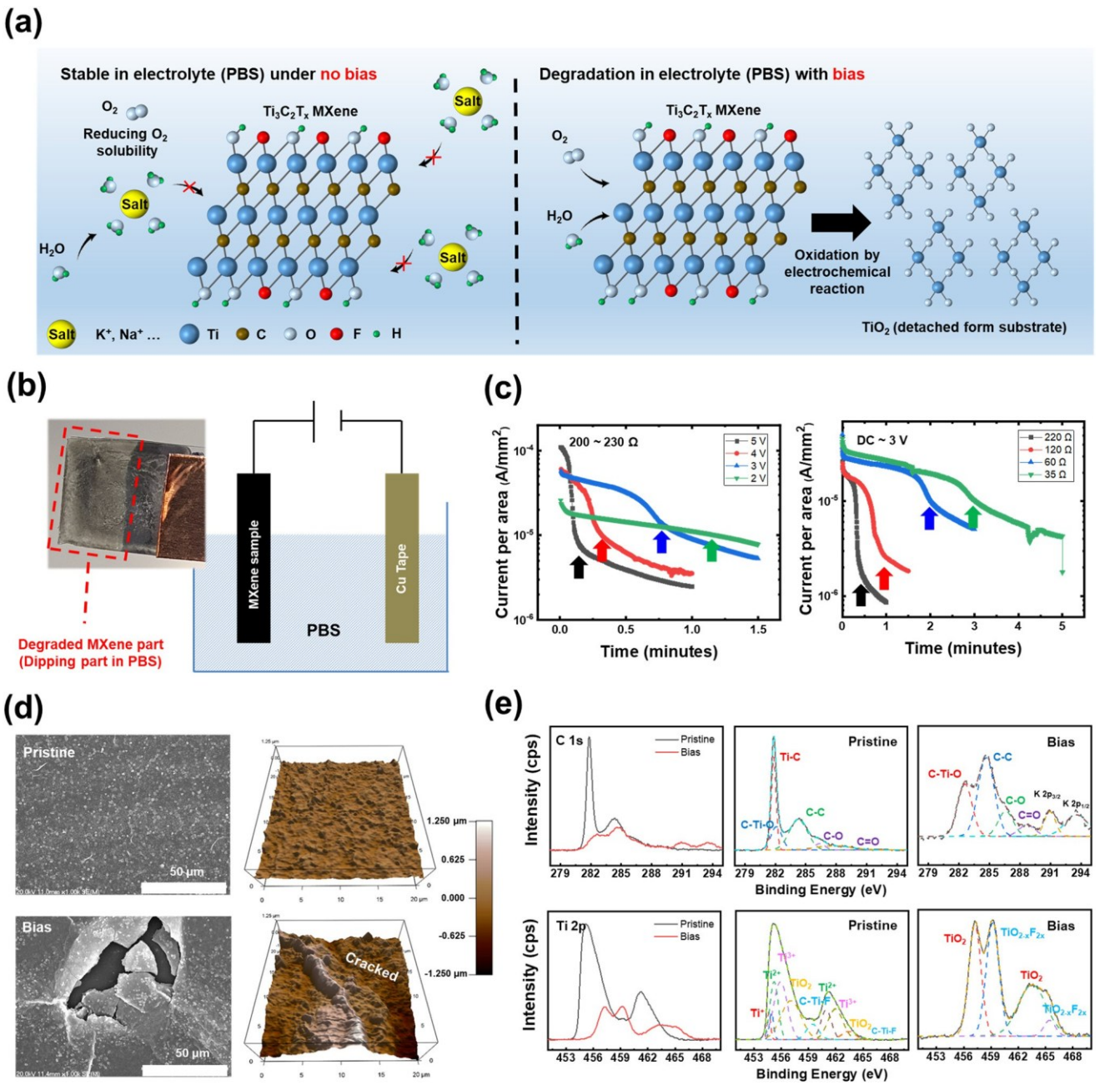

Fig. 2 (a) Schematic illustrations of MXene at an electrolytic cell under pristine and bias application conditions, (b) experimental set of the electrochemical reaction of the MXene layer, (c) influence of the applied potential on the opening behavior of the MXene valve at a fixed resistance range and influence of the MXene resistance (thickness) on the opening behavior under a fixed potential condition and (d) morphology results of MXene layers with SEM and AFM and pristine and bias application, and (e) C 1s and Ti 2p XPS spectra of MXene layers with pristine and bias application.

product.[12] Therefore, the higher voltage condition-induced rapid crevice corrosion leads to electrical isolation at MXene layers. The right graph in Fig. 2c also shows a correlation between the applied voltage and the electrolysis rate, in which the higher voltage, accompanied by lower MXene resistance, results in a more rapid electrolysis.

Fig. S5† and 2d exhibit the morphological analysis before/after electrolysis (applied DC: 3 V) by scanning electron microscopy (SEM) and atomic force microscopy (AFM) to demonstrate the presence of a controllable gate system. The continuous coverage of the MXene layer ensures a high conductivity of the thin film, while confirming that electrochemical reactions take place over the whole area. Fig. S5a† shows many cracks caused by the electrolyzed redox in the biased SEM image. Fig. S5b† indicates that the MXene flakes already detached from the substrate by magnified SEM and EDX, as well as AFM. The redox phenomenon between the electrolyte and the MXene interface was successfully carried

out under electric bias (the related chemical reaction is illustrated in the ESI†). According to the note in the ESI† in Fig. S5, TiO_2 was formed under the redox phenomenon and the MXene lamellae were dislodged from the surface to achieve the effect of opening the gate and releasing the drug.

Fig. 2e shows the fractions of the compounds before/after electrolysis by X-ray photoelectron spectroscopy (XPS). Changes depending on the presence or absence of electrical bias could be observed in both C 1s and Ti 2p XPS spectra. The C 1s XPS spectra of pristine MXene layers show various peaks with C–Ti, C–Ti–O, C–C, C–O, and C□O corresponding to 281.0 eV, 282.1 eV, 284.3 eV, 286.3 eV, and 288.0 eV, respectively.[33–35] Notably, the Ti–C peak, representing the main parts of MXene, distinctly disappeared, illustrating the transformation of compounds during the electrolysis process. Therefore, the graph after applying bias exhibits the peaks with C–Ti–O, C–C, C–O, and C□O, corresponding to 282.5 eV, 284.6 eV, 286.6 eV, and 288.6 eV, respectively. On the other hand, the data after applying bias showed that the Ti–C peak, which is the main backbone of MXene, was removed. The graph showed the peaks with C–Ti–O,

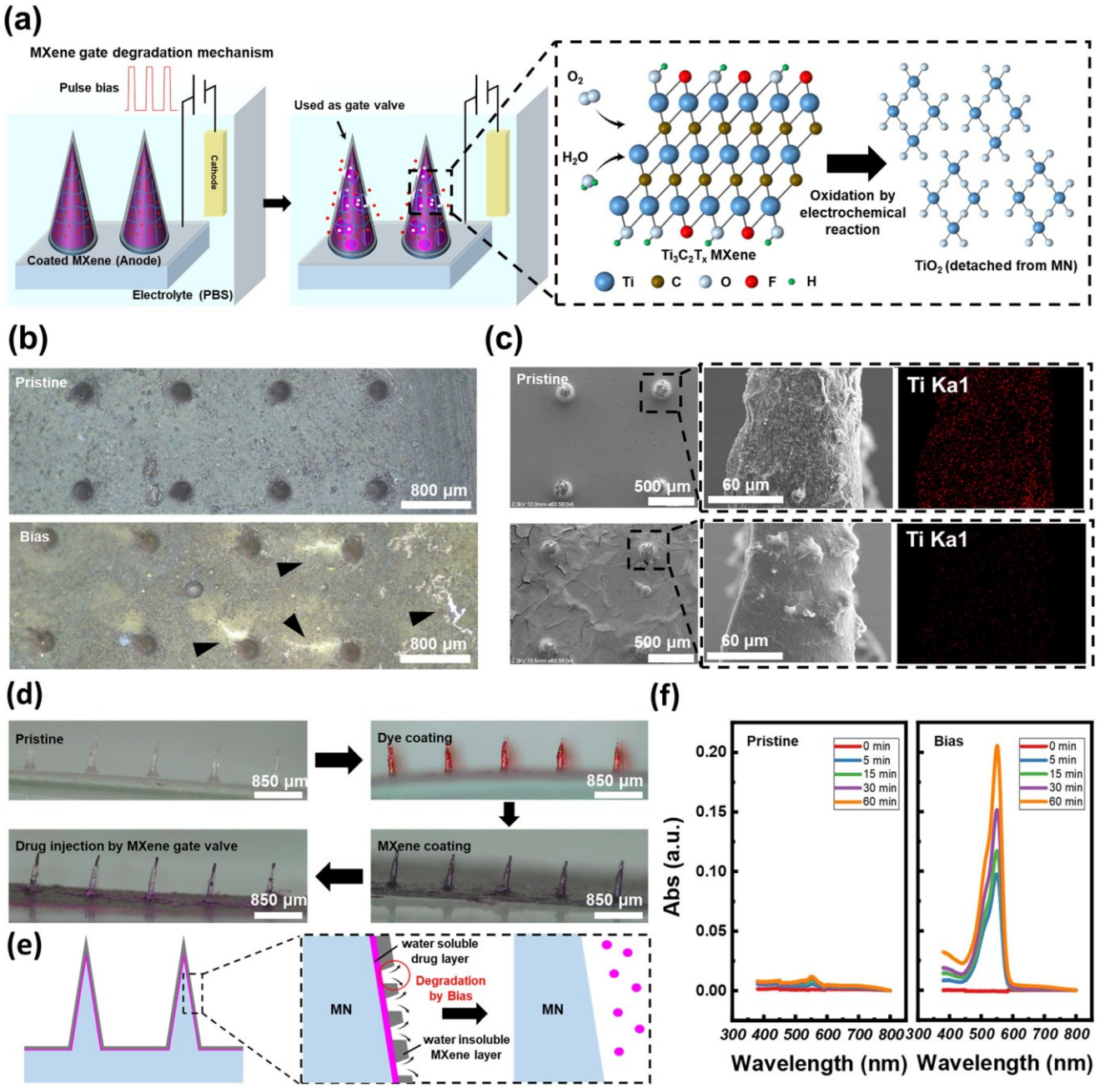

Fig. 3 (a) Operation mechanism of MXene based drug delivery devices, (b) top view OM and (c) top view/cross-section/Ti mapping SEM images of MXene layers with pristine and bias application, (d) cross-section OM images of the sequential process of the preparation and operation of MXene based drug delivery devices, (e) detailed image of the drug release of the prepared devices, and (f) UV-vis spectra measured with the collected solution depending on the time with samples using pristine and bias application conditions.

C–C, C–O, and C□O corresponding to 282.5 eV, 284.6 eV, 286.6 eV, and 288.6 eV, respectively. Similar trends were measured from the Ti 2p XPS data. While numerous metallic Ti-related peaks were observed in the pristine MXene sample, these metallic Ti peaks disappeared when a bias was applied in PBS solution. The Ti 2p XPS spectrum of pristine MXene featured dominant Ti^{n+} (n = 1–3) peaks, including Ti $2p_{3/2}$ at 454.6 eV, 455.2 eV, and 455.9 eV and Ti $2p_{1/2}$ at 460.8 eV and 461.9 eV. Additionally, smaller-scale Ti–O-related peaks were detected (Ti $2p_{3/2}$ at 457.0 eV and Ti $2p_{1/2}$ at 463.4 eV).[34] Following the bias-induced oxidation, the Ti 2p spectrum predominantly displayed large-scale Ti–O peaks, primarily indicative of TiO_2 formation, while the Ti^{n+} (n = 1–3) peaks were absent. Besides, Fig. S6† displays the complementary XPS analyses of O and F, related to the terminated groups (□O, –F, –OH) of MXene. O 1s reveals an augmentation in Ti–O_2-related peaks after applying bias to MXene, a finding that is parallel to the results observed in the C 1s and Ti 2p XPS spectra. XPS results collectively suggest that Ti_3C_2 is mostly converted into TiO_2 with the electrical bias, realizing electrically controlled gate opening.

Fig. 3 shows the MXene coating as the actively controlled gate for MNs to enable the drug release. It is confirmed that the redox phenomenon occurred well in MXene thin films depending on the electrical bias conditions. Drug delivery bioelectronics were prepared with double coating of rhodamine B and MXene through water processing. Fig. 3a exhibits the schematics of MXene-incorporated MN array's operation that can verify drug release under the control of electrical signals. Fig. 3b shows the optical microscope (OM) images before and after the electrical decomposition of the MXene layer with the MN array. The surface of the MXene layers on the MNs was corroded after a bias of 3 V was applied to the sample for 10 min. Corrosion cracks were numerous and were observed throughout the MNs and the surface (black arrow in the bias OM image). Fig. 3c shows the enlarged top-view and cross-section SEM images of the MXene-incorporated MNs before/after applying bias. From the top view, the pristine sample shows a very clean surface overall, but many obvious cracks appear on the surface of the sample after applying bias. Besides, from the cross-section images, EDX mapping, and SEM images, it can be seen that there are many aggregated MXene distributed in the MNs of the pristine sample, while the MNs of the biased sample show that most of the MXene has disappeared. This suggests that MXene is well deposited on the MNs and that it was possible to destroy it due to electrical signals even with three-dimensional structured MNs. Particularly, when an electrical signal is applied on the cross-section, most of the MXene is disrupted and detached. This suggests that coated MXene can be decomposed by the electrical signal when the device is fabricated by introducing the drug delivery material, thus allowing the drug under the coated MXene layer to be readily released.

To validate the generality of the model drug release, we used RhB (a water-soluble red dye) as the model drug, and coated it and MXene sequentially on the MN array. The coating process of MXene was conducted with drop-casting, because if the process is done by dipping like conventional coated MN fabrication, the water-soluble drug might be lost during processing.[26] Although it causes dissolution of some of the drug surface, this is trapped by the deposition of MXene, a low-dimensional material with a layered structure, and can form a conductive microneedle with excellent conductivity. Fig. 3d illustrates the cross-section OM images of each step from dye coating to MXene coating, and finally to the drug injection *via* the MXene gate. After applying the electrical bias, the residual materials on the MNs disappeared. This indicates that the drug in the MN portion has been successfully released. Fig. 3e illustrates the drug release mechanism briefly. The electrical bias can degrade the top MXene layer, allowing exposure of underlying RhB to the electrolyte through the cracks, and RhB was dissolved in water.[36]

Additionally, the MXene coating is kept stable in the electrolyte without the application of an electrical bias, which is necessary for enabling actively controlled drug release. As shown in Fig. S7a,† when only RhB was coated without MXene, RhB was released and diffused in water, whereas when MXene was additionally coated on RhB, the release was not visible. In particular, Fig. S7b† shows the complete MXene layers on MNs without applying electrical bias. Indeed, the stability of MXene in PBS solution was tested for 15 days as shown in Fig. S8.† According to the photograph, the MXene coated sample after immersing in PBS solution for 15 days was not much degraded with a high conductivity level. This indicates that the MXene sample without electrical bias still maintained the electrical conductivity level under ionic solution conditions. Fig. S9a† illustrates the experimental set to confirm the drug release by our devices. A small Petri dish was filled with a PBS solution (~50 ml), while an external electrical bias (total time 15 min) was applied to the MXene-coated MNs using copper tape. When an electrical bias was applied, gas was generated from the copper tape due to reduction. Fig. S9a† shows the drug released from the MXene-coated MNs due to oxidation. Accordingly, approximately 2 ml of PBS solutions containing the drug dispersed over time were collected as shown in Fig. S9b,† and UV-vis absorption measurements were conducted with these collected solutions. Fig. 3f presents the UV-vis absorption spectra of pristine and bias-applied cases, in which both cases show the absorption peak appearing at 550 nm.[37] However, the degree of drug release in the pristine case was much smaller than the degree of release in the case where a bias was applied. For a 1 hour period, less than 5% of the drug was released without applied bias (~0.011 in the UV-vis spectra) compared to the case where a bias was applied (~0.205 in the UV-vis spectra).

Fig. 4 shows the combination of different model drugs (RhB and sunset yellow FCF) to integrate into a single MN array, enabling the on-demand transformation and local-region customization of drug release with the actively controlled MXene gate. Notably, Fig. 4a shows that MXene-incorporated MNs patterning process with simple laser irradiation toward digital circuit fabrication. This manufacturing

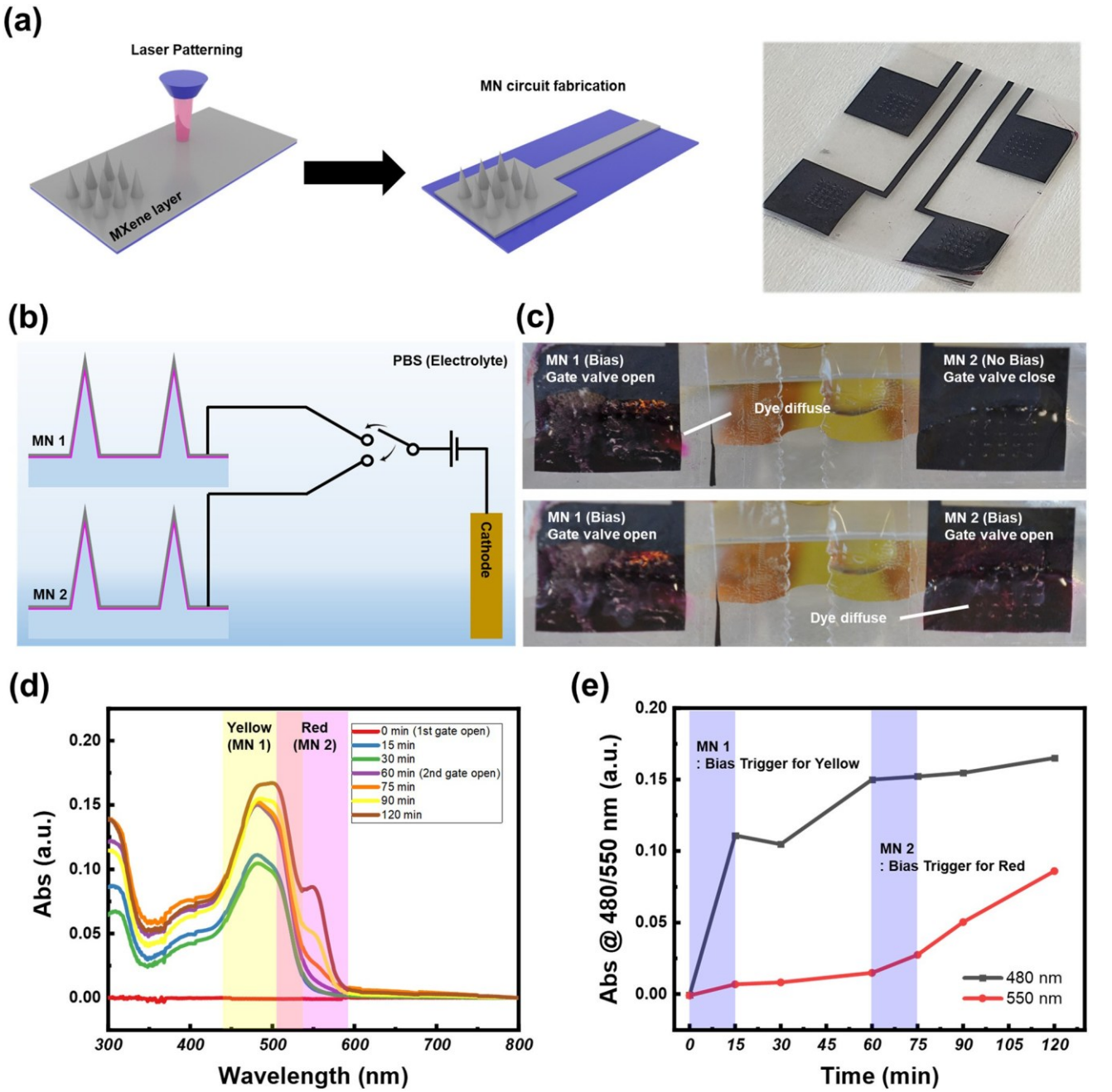

Fig. 4 (a) Fabrication process of MXene patterning and fabricated sample photograph, (b) schematic description of sequential release of drugs with two MN devices, (c) the picture of drug release conditions depending on the electrical bias, (d) UV-vis spectra measured with the collected solution for sequential drug delivery, and (e) peak intensities at 480 nm and 550 nm calculated from the UV-vis spectra.

process suggested that simple fabrication method which do not require conventional bioelectronic coatings (*e.g.*, Mo, Au, and Mg, *etc.*) through wafer-scale technologies or the cleanroom instruments. In particular, the ethyl cellulose substrate shows negligible absorption of the 1060 nm laser, and thus it can be effectively preserved during laser ablation. According to the previous work, MXene can be selectively ablated under the 1060 nm laser (laser patterning) due to the photothermal properties of MXene.[38] Thus, the substrate remains stable while the MXene is being shaped.

Fig. 4b depicts the fabrication of a multi-drug release device using two model drugs and the selective release of the drugs based on the site of application of a selective electrical bias. Fig. 4c demonstrates the regionally controlled drug release according to the respective bias applied. Briefly, if a bias was applied to MN 1 (left) and not to MN 2 (right), the MXene gate valve of MN 1 was opened whereas that of MN 2 was not opened. In this case, only the drug from MN 1 (yellow drug) was released and diffused. When a bias was applied to the MN 2 side, the closed MXene gate valve of MN

2 opened and the drug (red drug) was released and spread. Fig. 4c exhibits the UV-vis absorbance of the collected solution over time to confirm that the injection of the drugs was controlled according to the direction of the electrical signal (~3 V). After the MXene valves were opened sequentially, sunset yellow FCF and RhB were released by checking the UV-vis spectra at 480 nm and 550 nm. Fig. 4d compares the intensity of each peak at 480 nm and 550 nm wavelengths, confirming that the MXene coating is capable of achieving strictly controlled drug release w/wo bias application. Besides, multi-drug release MNs allow staged drug delivery, in which the second drug was released only after the second gate valve was opened, featuring the response and multifunctionality of the MXene-based MN drug delivery devices.

Fig. 5 shows the biocompatibility of MXene-incorporated MNs, featuring cytotoxicity *in vitro* while *in vivo* implants are buried under the porcine epidermis. MXene-incorporated MNs enable long-term minimal immunological responses and tissue reactions, mutually corroborating with the commercial Au traces. Fig. 5a exhibits that cardiomyocyte survival was higher in the MXene group, while Fig. 5b indicates that cardiomyocyte viability was less attenuated in the MXene group than in the other experimental groups. Fig. 5c shows the immunohistochemical analysis of tissues surrounding the implanted MXene and Au patches. Fig. 5d compares the corresponding quantification expressions in rat skin, making the less inflammatory MXene patch to induce fewer macrophages. Fig. 5e displays the quantification of the thickness of fibrotic tissues in rat skin, featuring that MXene induces less fibrosis than Au traces. Fig. 5f (Masson's) and 5g (H&E) present the extent of fibrosis in the surrounding tissue after two week-long porcine subcutaneous embeddings, respectively. Therefore, MXene-incorporated MNs exhibit biocompatibility and can fulfill the requirement of long-term biosafety and durability of bioelectronic implants.

3. Conclusion

In summary, we report novel bioelectronic microneedles (MNs) for drug delivery with an ethyl cellulose substrate and MXene gate valve for encapsulation of drugs. MXene ($Ti_3C_2T_x$), which is a highly conductive, stable, and biocompatible metallic material, was successfully deposited on the probes as the coating. MXene coatings have metal-like electrolyte properties with the capacity of an actively controlled gate valve and can release drugs *via* electrochemical/redox reactions through the application of a bias. In the absence of bias, MXene coating insulates the drug from contact with the outside electrolyte. Therefore, MXene-incorporated MNs achieve a strictly controlled release (w/wo) of the drug. Notably, the attribute of solution processability endows these structures with cost-effectiveness and sustainable operability. Furthermore, the MXene-incorporated MNs enable targeted transformation and region-specific customization. This advancement significantly enhances the structural complexity and efficacy of systems designed for the delivery of multiple drugs in a temporally programmable fashion.

4. Experimental section

Materials

Ethyl cellulose and RhB were obtained from Thermo Fisher Scientific. Toluene, isopropyl alcohol (IPA), and ethyl alcohol were purchased from Sigma Aldrich. A SYLGARD 184 silicone elastomer kit (PDMS) and phosphate buffer solution (PBS) were obtained from Dow Corning. Water dissolved MXene (Ti_3C_2) solution (10 mg ml^{-1}) was bought from FEYNMAN Nano (at China). Sunset yellow FCF was purchased from Bidepharm (China). Deionized water was obtained from Havenlab. All other reagents were purchased as analytical grade reagents and used according to the instructions.

MN and coated MN preparation

Before the preparation of polymer MN patches, an MN mold was firstly fabricated with PDMS. The SYLGARD 184 silicone elastomer kit (well mixed and centrifuged; 10 : 1 of the base and crosslinker) was applied on a glass Petri dish, and was stored under vacuum conditions (~50 mmHg) for 30 minutes to eliminate air in the mixture. Then, the elastomer kit was stored at 60 °C and under ambient air conditions for 3 hours to achieve full crosslinking. For making the MN mold, the UV laser was applied on the prepared PDMS. To remove the PDMS residuals by the laser irradation, the mold was ultrasonically washed using IPA for 10 minutes. The homogeneous solution with ethyl cellulose solution was obtained by dissolving it in a 10 wt% toluene and ethyl alcohol mixture (1 : 1 wt ratio). The fabricated solution was directly applied on the prepared PDMS MN mold, and evacuated for 15 minutes to allow the applied solution to fully penetrate into the mold. Afterwards, the mold, to which the solution was applied, was dried in air for 1 day. Because the produced MNs were made with ethyl cellulose, they are relatively hydrophobic. To improve the surface adhesion of the MN patches, oxygen plasma treatment was applied for about 2 minutes. Then, the RhB or sunset yellow FCF solution dissolved in deionized water was applied on the MN patch by drop casting. After the solvent was completely evaporated, diluted MXene solution (~1 mg ml^{-1}) was applied to make the MXene-coated ethyl cellulose MN patches. Laser scribing was conducted with an SFX Laser Engraver JPT Fiber Laser Marking Machine.

Characterization

The morphology of MXene and MN samples was examined using an OM, SEM (Hitachi S-4700 with EDX), and AFM (Asylum Research MFP3D). For conducting SEM, the MN samples were coated with a thin layer of platinum (~5 nm) by sputtering. The electrochemical reaction/degradation with the MXene layer was conducted with LabVIEW software and equipment (NI-USB 4065, National Instruments). Under the

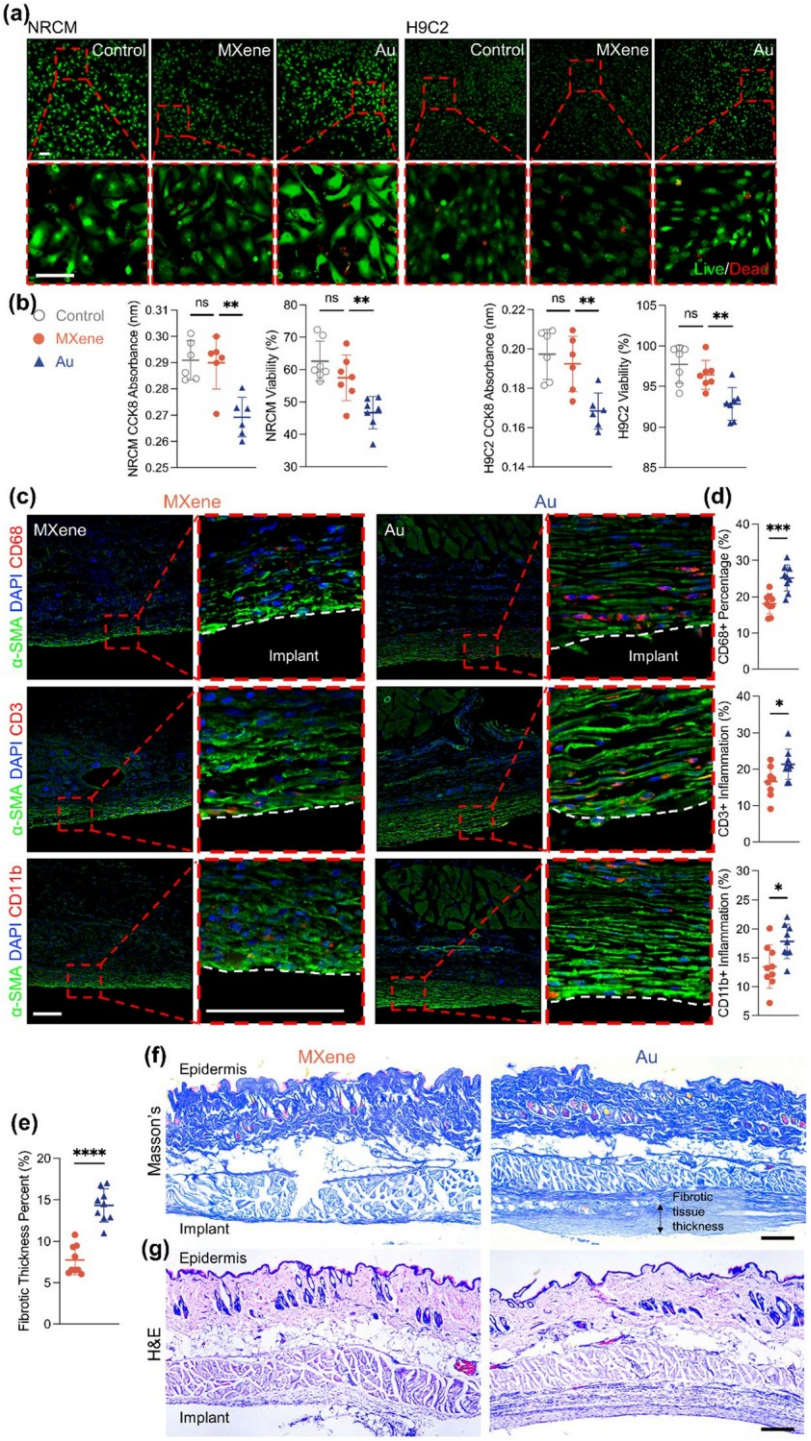

Fig. 5 (a) Cytotoxicity analysis of the control, OBXene, and Au implants (dimension: 2.5 mm × 2.5 mm × 50 μm, $L \times W \times H$) in neonatal rat cardiomyocytes (NRCMs) and H9C2 cardiomyocytes, indicating higher cardiomyocyte viability in the MXene group. Green indicates live cells, while red indicates dead cells. (b) Cell counting kit 8 (CCK8) analysis of NRCM and H9C2 showed less cardiomyocyte viability attenuation in the MXene group than in the other experimental groups. Quantification of NRCM and H9C2 viability did not show a significant decrease in the MXene group compared to the control, while Au induced a significant decrease in cell viability compared to MXene. (c) Immunohistochemical analysis of tissues surrounding the implanted MXene and Au patches. The tissues were stained with α-smooth muscle actin (α-SMA) (smooth muscle and myofibroblast), DAPI (nucleus), and inflammatory markers: CD68 (macrophages), CD3 (T cells), and CD11b (neutrophils). (d) Quantification of inflammatory marker expression in rat skin indicating that the MXene patch induced fewer macrophages (CD68), T cells (CD3), and neutrophils (CD11b) than the Au patch. (e) Quantification of rat skin fibrotic tissue thickness percent indicating that MXene induced less fibrotic tissue compared to Au. (f and g) Microscopy images of the surrounding tissues with (e) Masson's trichrome staining indicating lower fibrotic tissue thickness in the MXene group and (f) hematoxylin and eosin (H&E) staining indicating fewer inflammatory cells in the MXene group. Scale: a and c: 100 μm; e and f: 400 μm. All data are mean ± SD. For normally distributed datasets, 1-way ANOVA (b) or unpaired 2-tailed Student's t test (d and e) with Tukey correction was performed. Significance: ns indicates $P > 0.5$, $^{*}P \leq 0.05$, $^{**}P \leq 0.01$, $^{***}P \leq 0.001$, $^{****}P \leq 0.0001$.

DC current conditions, the current levels were measured with an electrical analyzer. The experiment was carried out in a two-electrode system, where the counter electrode was 3 M pristine copper tape. Multiple drug delivery microneedles were tested with electrochemical bias application utilizing the PowerLab equipment (16SP ADInstruments). Selective bioelectronics confirmed the degree of drug release by independently applying voltage over time. Besides, the PBS solution, in which the drug released over time had diffused, was extracted and the UV-vis absorption was confirmed using a UV-vis spectrometer (Scilogex SCI-UV1000 UV/vis).

Material cytotoxicity *in vitro*

Both MXene and Au were fabricated into 1 cm^2 sheets (~0.2 mm thick). The materials were sterilized using an autoclave prior to *in vitro* assays. Neonatal rat cardiomyocytes (NRCMs) were isolated from 1 day-old Sprague Dawley (SD) neonatal rats. We diluted the cell suspension in Iscove's modified Dulbecco's medium (IMDM) with 10% fetal bovine serum (FBS) into 2×10^5 cells per mL for optimal NRCM plating efficiency. H9C2 rat embryonic cardiomyocytes were plated at 10^4 cells per mL due to their high proliferation rate. NRCMs and H9C2s were cultured for 48 hours, and then MXene and Au patches were placed in the cell culture for 24 hours. For viability analysis, NRCMs and H9C2s were plated in 8-well slides (Millicell). Each material was placed into 3 wells for NRCM slides and H9C2 slides. There were 3 control wells with no materials for each cell type. A LIVE/DEAD viability/cytotoxicity kit (Thermo Fisher Scientific) was used to determine the cell viability of NRCM and H9C2.

Material biocompatibility in rat and porcine models

For all *in vivo* experiments, compliance with animal welfare standards was maintained throughout all animal experiments, aligning with the guidelines outlined by the Institutional Animal Care and Use Committee (IACUC #22-128) at the North Carolina State University and the NIH Guide for the Care and Use of Laboratory Animals. Two *in vivo* models were used for biocompatibility studies. Sprague Dawley rats were used for electrode material biocompatibility assays. A Yorkshire pig was used to test the biocompatibility of the MXene-coated microneedle array. MXene and Au were fabricated into 1 cm by 3 cm sheets (~0.2 mm thick). The materials were sterilized using an autoclave prior to *in vivo* assays. The materials were implanted subcutaneously into SD rats ($n = 3$) for 7 days. After the endpoint, the animals were sacrificed with inhalation of CO_2 and the skin tissue was collected for further analysis. A sham skin section was also collected as the control. Rat and pig skin tissues were embedded as frozen tissues and sectioned using a cryostat. A total of three assays were conducted: immunohistochemistry, Masson's trichrome histology, and hematoxylin and eosin (H&E) histology.

Statistical analysis

All results are expressed as mean ± SD. A comparison between the two groups was performed with a parametric *t*-test. Comparisons among more than two groups were performed using a one-way analysis of variance (ANOVA) followed by the *post hoc* Bonferroni test. Comparisons between more than two groups and more than one categorical variable were performed using a two-way analysis of variance (ANOVA) followed by the *post hoc* Bonferroni test. Differences were considered statistically significant when $P < 0.05$.

Conflicts of interest

There are no conflicts to declare.

Acknowledgements

This work was supported by start-up funds from the University of North Carolina at Chapel Hill and funds from the National Science Foundation (award no. ECCS-2139659). Research reported in this publication was also supported by the National Institute of Biomedical Imaging and Bioengineering at the National Institutes of Health under award number 1R01EB034332-01.

References

1 Y. Wang, Z. Chen, B. Davis, W. Lipman, S. Xing, L. Zhang, T. Wang, P. Hafiz, W. Xie, Z. Yan, Z. Huang, J. Song and W. Bai, *Nat. Commun.*, 2024, 15, 511.
2 Z. Zhu, J. Wang, X. Pei, J. Chen, X. Wei, Y. Liu, P. Xia, Q. Wan, Z. Gu and Y. He, *Sci. Adv.*, 2023, 9, eadh2213.
3 Y. Liu, R. Menon, A. Putcha, K. Huang, L. Bonilla, R. Vora, J. Li, L. Zhang, Y. Wang, L. Fletcher, A. Lassiter, C. Huang, J. B. Buse, K. Cheng and W. Bai, *Adv. Mater. Technol.*, 2022, 7, 2200468.
4 I. Armenia, C. Cuestas Ayllón, B. Torres Herrero, F. Bussolari, G. Alfranca, V. Grazú and J. Martínez de la Fuente, *Adv. Drug Delivery Rev.*, 2022, 191, 114584.
5 H. Ji, M. Wang, Y. Wang, Z. Wang, Y. Ma, L. Liu, H. Zhou, Z. Xu, X. Wang, Y. Chen and X. Feng, *npj Flexible Electron.*, 2023, 7, 46.
6 T. Waghule, G. Singhvi, S. K. Dubey, M. M. Pandey, G. Gupta, M. Singh and K. Dua, *Biomed. Pharmacother.*, 2019, 109, 1249–1258.
7 J. H. Jung and S. G. Jin, *J. Pharm. Invest.*, 2021, 51, 503–517.
8 H. Amani, M.-A. Shahbazi, C. D'Amico, F. Fontana, S. Abbaszadeh and H. A. Santos, *J. Controlled Release*, 2021, 330, 185–217.
9 T. Peng, Y. Chen, W. Hu, Y. Huang, M. Zhang, C. Lu, X. Pan and C. Wu, *Engineering*, 2023, 30, 170–189.
10 W. Chen, J. Wainer, S. W. Ryoo, X. Qi, R. Chang, J. Li, S. H. Lee, S. Min, A. Wentworth, J. E. Collins, S. Tamang, K. Ishida, A. Hayward, R. Langer and G. Traverso, *Sci. Adv.*, 2022, 8, eabk1792.

11 H. Chang, S. W. T. Chew, M. Zheng, D. C. S. Lio, C. Wiraja, Y. Mei, X. Ning, M. Cui, A. Than, P. Shi, D. Wang, K. Pu, P. Chen, H. Liu and C. Xu, *Nat. Biomed. Eng.*, 2021, 5, 1008–1018.
12 J. Koo, S. B. Kim, Y. S. Choi, Z. Xie, A. J. Bandodkar, J. Khalifeh, Y. Yan, H. Kim, M. K. Pezhouh, K. Doty, G. Lee, Y.-Y. Chen, S. M. Lee, D. D'Andrea, K. Jung, K. Lee, K. Li, S. Jo, H. Wang, J.-H. Kim, J. Kim, S.-G. Choi, W. J. Jang, Y. S. Oh, I. Park, S. S. Kwak, J.-H. Park, D. Hong, X. Feng, C.-H. Lee, A. Banks, C. Leal, H. M. Lee, Y. Huang, C. K. Franz, W. Z. Ray, M. MacEwan, S.-K. Kang and J. A. Rogers, *Sci. Adv.*, 2020, 6, eabb1093.
13 S. Liu, Z. Jia, F. Yang, T. Ning, X. Gu, X. Niu and Y. Fan, *Adv. Funct. Mater.*, 2023, 33, 2215034.
14 Y. Gogotsi and B. Anasori, *ACS Nano*, 2019, 13, 8491–8494.
15 X. Zhao, A. Vashisth, E. Prehn, W. Sun, S. A. Shah, T. Habib, Y. Chen, Z. Tan, J. L. Lutkenhaus, M. Radovic and M. J. Green, *Matter*, 2019, 1, 513–526.
16 Y. Li, S. Huang, C. Wei, C. Wu and V. N. Mochalin, *Nat. Commun.*, 2019, 10, 3014.
17 K. Rasool, M. Helal, A. Ali, C. E. Ren, Y. Gogotsi and K. A. Mahmoud, *ACS Nano*, 2016, 10, 3674–3684.
18 Y. Nie, J. Huang, S. Ma, Z. Li, Y. Shi, X. Yang, X. Fang, J. Zeng, P. Bi, J. Qi, S. Wang, Y. Xia, T. Jiao, D. Li and M. Cao, *Appl. Surf. Sci.*, 2020, 527, 146915.
19 S. Lin, H. Lin, M. Yang, M. Ge, Y. Chen and Y. Zhu, *Nanoscale*, 2020, 12, 10265–10276.
20 H. Lin, S. Gao, C. Dai, Y. Chen and J. Shi, *J. Am. Chem. Soc.*, 2020, 142, 10567.
21 S. Abdolhosseinzadeh, X. Jiang, H. Zhang, J. Qiu and C. Zhang, *Mater. Today*, 2021, 48, 214–240.
22 M. Bariya, Z. Shahpar, H. Park, J. Sun, Y. Jung, W. Gao, H. Y. Y. Nyein, T. S. Liaw, L.-C. Tai, Q. P. Ngo, M. Chao, Y. Zhao, M. Hettick, G. Cho and A. Javey, *ACS Nano*, 2018, 12, 6978–6987.
23 H. Seddiqi, E. Oliaei, H. Honarkar, J. Jin, L. C. Geonzon, R. G. Bacabac and J. Klein-Nulend, *Cellulose*, 2021, 28, 1893–1931.
24 B. He, X. Liu, S. Qi, R. Zheng, M. Chang, Q. Lin and J. Ren, *Curr. Med. Chem.*, 2021, 28, 8296–8318.
25 A. S. Sharova, F. Modena, A. Luzio, F. Melloni, P. Cataldi, F. Viola, L. Lamanna, N. F. Zorn, M. Sassi, C. Ronchi, J. Zaumseil, L. Beverina, M. R. Antognazza and M. Caironi, *Nanoscale*, 2023, 15, 10808–10819.
26 Y. Chen, B. Z. Chen, Q. L. Wang, X. Jin and X. D. Guo, *J. Controlled Release*, 2017, 265, 14–21.
27 G. W. M. Vandermeulen, A. Boarino and H.-A. Klok, *J. Polym. Sci.*, 2022, 60, 1797–1813.
28 A. C. Lima, N. Pereira, C. Ribeiro, S. Lanceros-Mendez and P. Martins, *ACS Sustainable Chem. Eng.*, 2022, 10, 4122–4132.
29 H. Alnoor, A. Elsukova, J. Palisaitis, I. Persson, E. N. Tseng, J. Lu, L. Hultman and P. O. Å. Persson, *Mater. Today Adv.*, 2021, 9, 100123.
30 Q. Zhao, Q. Zhu, Y. Liu and B. Xu, *Adv. Funct. Mater.*, 2021, 31, 2100457.
31 J. Kim, Y. Yoon, S. K. Kim, S. Park, W. Song, S. Myung, H.-K. Jung, S. S. Lee, D. H. Yoon and K.-S. An, *Adv. Funct. Mater.*, 2021, 31, 2008722.
32 X. Wang, Z. Wang and J. Qiu, *Angew. Chem., Int. Ed.*, 2021, 60, 26587–26591.
33 L. Wang, H. Zhang, B. Wang, C. Shen, C. Zhang, Q. Hu, A. Zhou and B. Liu, *Electron. Mater. Lett.*, 2016, 12, 702–710.
34 B. Ahmed, D. H. Anjum, M. N. Hedhili, Y. Gogotsi and H. N. Alshareef, *Nanoscale*, 2016, 8, 7580–7587.
35 L. Zhang, G. Chen, M. N. Hedhili, H. Zhang and P. Wang, *Nanoscale*, 2012, 4, 7038–7045.
36 Y. Zhang, F. Liu, Y. Zhang, J. Wang, D. D'Andrea, J. B. Walters, S. Li, H.-J. Yoon, M. Wu, S. Li, Z. Hu, T. Wang, J. Choi, K. Bailey, E. Dempsey, K. Zhao, A. Lantsova, Y. Bouricha, I. Huang, H. Guo, X. Ni, Y. Wu, G. Lee, F. Jiang, Y. Huang, C. K. Franz and J. A. Rogers, *Proc. Natl. Acad. Sci. U. S. A.*, 2023, 120, e2217734120.
37 U. R. Gandra, R. Courjaret, K. Machaca, M. Al-Hashimi and H. S. Bazzi, *Sci. Rep.*, 2020, 10, 19519.
38 S. Kyrylenko, O. Gogotsi, I. Baginskiy, V. Balitskyi, V. Zahorodna, Y. Husak, I. Yanko, M. Pernakov, A. Roshchupkin, M. Lyndin, B. B. Singer, V. Buranych, A. Pogrebnjak, O. Sulaieva, O. Solodovnyk, Y. Gogotsi and M. Pogorielov, *ACS Appl. Mater. Interfaces*, 2022, 14, 28683–28696.

